

Iron-Ion Bolted VOPO₄·2H₂O as an Aqueous Fe-ion Battery Electrode

Yunkai Xu, Xianyong Wu, Sean K. Sandstrom, Jessica J. Hong, Heng Jiang, Xin Chen, Xiulei

Ji*

Y. Xu, Dr. X. Wu, S. Sandstrom, J. Hong, Dr. H. Jiang, Dr. X. Chen, Prof. X. Ji

Department of Chemistry

Oregon State University

Corvallis, OR 97331, USA

E-mail: david.ji@oregonstate.edu

Keywords: aqueous electrolytes, iron metal battery, vanadium oxyphosphate, ion bolting

Abstract

Iron ion batteries using Fe²⁺ as a charge carrier have yet to be widely explored, and there lack high-performing Fe²⁺ hosting cathode materials to couple with the iron metal anode. Here, we demonstrate that VOPO₄·2H₂O can reversibly host Fe²⁺ with a high specific capacity of 100 mAh/g and stable cycling performance, where 68% of the initial capacity is retained over 800 cycles. In sharp contrast, VOPO₄·2H₂O's capacity of hosting Zn²⁺ fades precipitously over tens of cycles. VOPO₄·2H₂O stores Fe²⁺ with a unique mechanism, where upon contacting the electrolyte by the VOPO₄·2H₂O electrode, Fe²⁺ ions from the electrolyte get oxidized to Fe³⁺ ions that are inserted and trapped in the VOPO₄·2H₂O structure in an electroless redox reaction. The trapped Fe³⁺ ions, thus, bolt the layered structure of VOPO₄·2H₂O, which prevents it from dissolution into the electrolyte during (de)insertion of Fe²⁺. The findings offer a new strategy to use a redox-active ion charge carrier to stabilize the layered electrode materials.

1. Introduction

Global prosperity demands energy security that entails reliable energy storage systems with inerrable safety.^[1-4] Recently, aqueous batteries that employ metal anodes have attracted much attention.^[5-8] The emerging aqueous batteries differ from the well-established alkaline metal

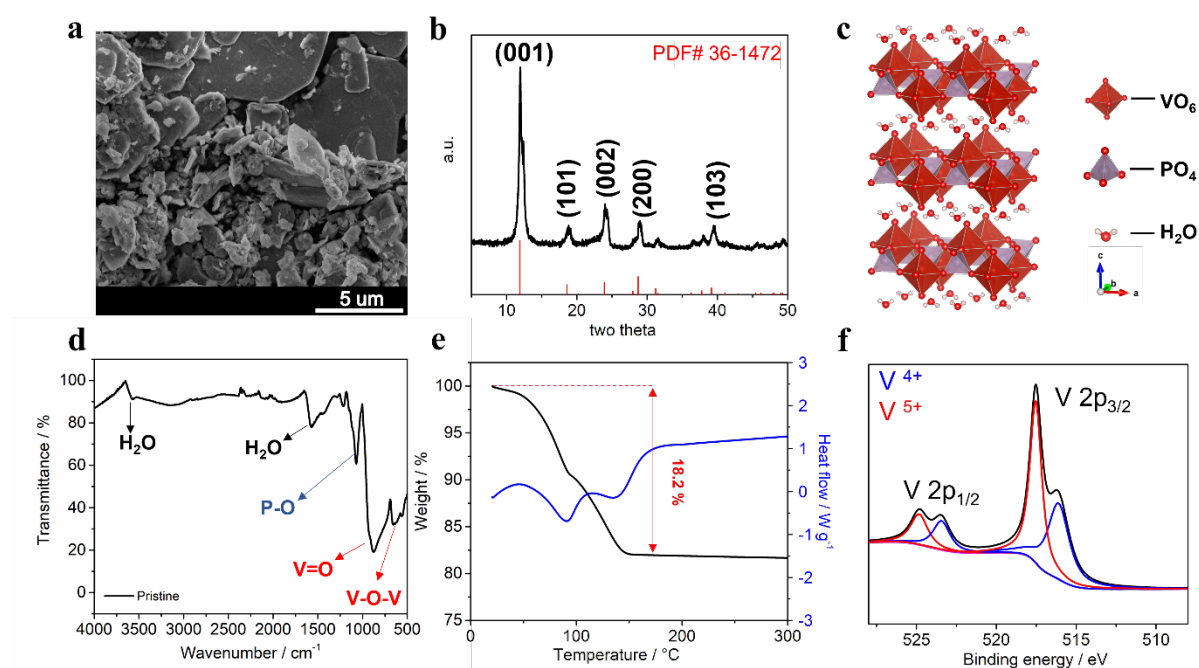
1 batteries, many of which are primary batteries;^[1] new aqueous batteries often employ neutral
2 or mildly acidic electrolytes that exhibit a wider electrochemical stability window.^[9, 10]
3 Recently, the field has been inundated with reports of progress made on zinc metal anode that
4 has many attributes.^[11-16] Nevertheless, batteries that employ an iron metal anode have been
5 left out despite iron's high specific capacity of 960 mAh/g and exceedingly low price of \$60
6 per tonne in contrast to \$2600 for zinc.¹⁷ Moreover, Fe possesses a higher M^{2+}/M redox
7 potential of -0.44 V (vs SHE, hereafter) compared to -0.76 V for Zn^{2+}/Zn , which promises no
8 or a lower extent of hydrogen evolution reaction (HER) depending on the pH value of the
9 electrolyte.^[17,18] The history of iron batteries dates back to the NiFe battery, which was
10 patented by in 1901 and commercialized soon afterward by the Edison Storage Battery
11 Company.^[19] In the NiFe battery, hydroxide ions serve as the charge carrier, instead of Fe^{2+} ,
12 for the operation of both cathode and anode.^[20,21,22]

13 Despite the advantages, Fe-ion batteries remain underexplored, particularly with fewer
14 Fe^{2+} -hosting cathode materials reported than the Zn^{2+} -hosting cathodes, *e.g.*, MnO_2 , V_2O_5 ,
15 VS_x , Prussian blue, and polyphosphates.^[23-25] Recently, our group reported the performance of
16 "insoluble" Prussian blue (IPB) ($Fe^{3+}[Fe^{2+}(CN)_6]_{0.73} \square_{0.27} \cdot 3.6H_2O$) that delivers a stable
17 specific capacity of 60 mAh/g and an average potential of 0.75 V versus Fe^{2+}/Fe .¹⁷ Studies
18 were extended to a few other materials for Fe^{2+} storage, which, unfortunately, encountered
19 issues, where the capacity of V_2O_5 fades quickly, MnO_2 shows a large overpotential (~ 0.5 V),
20 and both $FePO_4$ and sulfur exhibit low average discharge potentials.^[17, 26] Sundara *et al.*
21 reported a non-aqueous rechargeable Fe battery that comprises a V_2O_5 cathode and 1 M
22 hydrated $Fe(ClO_4)_2$ in tetraethylene glycol dimethylether (TEGDME) as an electrolyte.^[27] In
23 this non-aqueous electrolyte, the V_2O_5 cathode suffers a larger overpotential and lower
24 reversibility compared to its performance in the aqueous electrolytes.

25 Herein, we report the promising performance of $VOPO_4 \cdot 2H_2O$ as a cathode for Fe-ion
26 batteries, which delivers a specific capacity of 100 mAh/g at an average potential of ~ 0.6 V vs

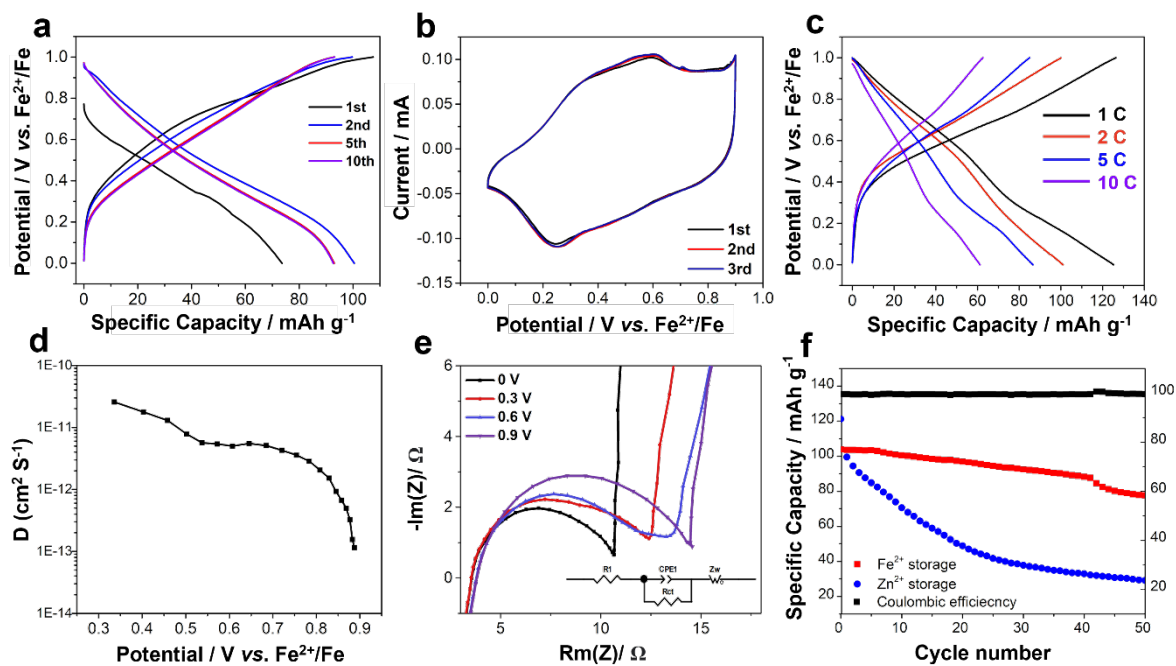
1 Fe^{2+}/Fe . Most importantly, $\text{VOPO}_4 \cdot 2\text{H}_2\text{O}$ does not suffer fast capacity fading in the Fe^{2+}
 2 electrolytes by retaining 68% of its capacity over 800 cycles. Nevertheless, when hosting
 3 Zn^{2+} , $\text{VOPO}_4 \cdot 2\text{H}_2\text{O}$ suffers rapid dissolution and capacity fading in aqueous electrolytes,
 4 which is a known challenge.^[13, 28, 29] To avoid electrode dissolution, Wang and Xu *et al.* used
 5 an acetonitrile-based electrolyte that has 1% of water.^[12] Srinivasan *et al.* strengthened the
 6 structure of $\text{VOPO}_4 \cdot 2\text{H}_2\text{O}$ by the pre-insertion of polypyrrole, which, unfortunately, still
 7 cannot stabilize the capacity of $\text{VOPO}_4 \cdot 2\text{H}_2\text{O}$ in pure aqueous electrolytes, albeit this
 8 approach is more effective in a hybrid aqueous/non-aqueous electrolyte.^[13] In this study, we
 9 found that $\text{VOPO}_4 \cdot 2\text{H}_2\text{O}$ favors the Fe^{2+} storage, where its structure is stabilized by the initial
 10 spontaneous incorporation and oxidation of Fe^{2+} at open circuit voltage (OCV), and the
 11 trapped Fe^{3+} in the structure bolts the structure of $\text{VOPO}_4 \cdot 2\text{H}_2\text{O}$ for reversible Fe^{2+} hosting.

12 2. Results and Discussion



13
 14 **Figure 1** Characterization of $\text{VOPO}_4 \cdot 2\text{H}_2\text{O}$. (a) SEM image of the as-synthesized
 15 $\text{VOPO}_4 \cdot 2\text{H}_2\text{O}$. (b) XRD pattern. (c) The schematic structure. (d) FTIR spectrum. (e) TGA
 16 curve. (f) XPS spectrum.

1 The layered $\text{VOPO}_4 \cdot 2\text{H}_2\text{O}$ was synthesized via a well-established reflux method, with
2 details provided in the experimental section.^[30] **Figure 1a** shows the SEM image of the as-
3 synthesized material, which comprises aggregations of flakes with particle sizes ranging from
4 ca. 1 to 10 μm . The X-ray diffraction (XRD) pattern (**Figure 1b**) indicates a phase-pure
5 product, where the peaks can be indexed to $\text{VOPO}_4 \cdot 2\text{H}_2\text{O}$ (PDF# 36-1472) with the tetragonal
6 P4/n space group.^[31] **Figure 1c** schematically shows the crystal structure, where the VO_6
7 octahedra and PO_4 tetrahedra share corners, thus constructing a layered structure. The Fourier
8 transform infrared (FTIR) spectrum confirms the presence of lattice water in the structure
9 (**Figure 1d**). The peak at 3580 cm^{-1} and the hump around 3100 cm^{-1} are assigned to the
10 water's stretching modes, ν_{OH} . The one at the higher wavenumber corresponds to water that is
11 not fully hydrogen bonded, and the one at the lower wavenumber can be assigned to the
12 lattice water molecules in the VOPO_4 structure. The peak at 1580 cm^{-1} corresponds to the
13 bending mode of water, ν_{HOH} , which is much red-shifted. The mass loss of $\text{VOPO}_4 \cdot 2\text{H}_2\text{O}$ by
14 18.2 wt.% in the thermogravimetric analysis (TGA) suggests the presence of two lattice water
15 molecules per formula of VOPO_4 (**Figure 1e**), and two endothermic peaks indicate two types
16 of water with different chemical environments, where one type as surface water evaporates at
17 a relatively low temperature, and the other type as the lattice water molecules evaporates at a
18 higher temperature due to the interaction with the electrode lattice. The Fourier-transform
19 infrared (FTIR) spectrum reveals the vibrations of a polyanionic network, where the signal at
20 680 cm^{-1} is assigned to the V-O-V extension vibration, the peak at 950 cm^{-1} corresponds to
21 the V=O stretching motion, and the peak at 1080 cm^{-1} pertains to the P-O stretching of the
22 PO_4^{3-} groups.^[30] X-ray photoelectron spectroscopy (XPS) results suggest that the average
23 vanadium valence state is +4.7 (**Figure 1f**). However, XPS is a surface technology; thus, the
24 oxidation state lower than +5 could be attributed to the surface defects of oxygen and
25 phosphate ions. The full XPS spectrum is provided in **Figure S1**, which confirms the
26 existence of other elements such as phosphorous and oxygen.



1
2 **Figure 2.** Electrochemical performance of VOPO₄·2H₂O. (a) GCD potential profiles at 1 C (1
3 C = 100 mA/g). (b) CV curves at a scan rate of 0.1 mV/s. (c) GCD potential profiles at
4 different C-rates. (d) Calculated diffusion coefficients as a function of potentials from the
5 GITT results. (e) EIS spectra at different state of charge (SOC). (f) Cycling performance for
6 Zn storage (discharge capacity) and Fe storage (discharge capacity) with Coulombic
7 efficiency (CE) of Fe²⁺ storage at 1 C.

8 The electrochemical properties of VOPO₄·2H₂O were evaluated by using 1 M aqueous
9 FeSO₄ (pH value of 5) as the electrolyte and metallic Fe powder as the counter electrode. It
10 should be noted that the study on Fe metal anode in this electrolyte has been reported by our
11 group previously.^[17] As shown in **Figure 2a**, the galvanostatic charge-discharge (GCD)
12 cycling of (de)insertion of Fe²⁺ in VOPO₄·2H₂O displays largely sloping potential profiles,
13 which is different from the results of Zn²⁺ storage in VOPO₄·2H₂O.^[5, 13] The first discharge
14 exhibits a specific capacity of 75 mAh/g, the following charge delivers a capacity of 100
15 mAh/g, and the second discharge exhibits a capacity of 98 mAh/g. For mildly acidic aqueous
16 electrolytes (pH value of 5 for 1 M FeSO₄ here), it is necessary to determine whether the
17 storage of protons contributes much to the observed capacity. From a control experiment of

1 using 3 mM H₂SO₄ (pH = 5) as the electrolyte (**Figure S2**), a limited reversible capacity of 13
2 mAh/g is observed, indicating that Fe²⁺ storage is mainly responsible for the observed
3 capacity and the proton storage plays a minor role. Energy Dispersive X-Ray Spectroscopy
4 (EDX) in **Figure S3** shows a homogeneous existence of Fe element in the discharged
5 electrode.

6 Cyclic voltammetry (CV) (**Figure 2b**) of Fe²⁺ storage in VOPO₄·2H₂O displays broad
7 peaks. The CV curves of the first three cycles are nearly identical, which again suggests the
8 good reversibility of Fe²⁺ (de)intercalation in VOPO₄·2H₂O over cycling. The lack of well-
9 resolved CV peaks and the quasi-rectangular shape of the CV curves liken the behavior here
10 to that of pseudocapacitive electrode materials.^[32-35] The kinetics of the Fe²⁺ storage in the
11 VOPO₄·2H₂O electrode can be evaluated by calculating the *b*-values of the peak currents
12 using the following equation:

$$13 \quad i = av^b \quad (1)$$

14 where *a* is a coefficient that is simplified from $i = k_1v + k_2v^{1/2}$. An ideal capacitive behavior
15 would give rise to a *b* value of 1, and an ideal diffusion-controlled process would lead to a *b*
16 value of 0.5.^[36, 37] **Figure S4** show that the cathodic and anodic current maxima exhibit *b*
17 values of 0.79 and 0.88, respectively, which tells a good extent of the capacitive behavior.
18 However, a capacitive behavior cannot always be translated to faster rate capability, which is
19 epitomized here. At 10 C, the electrode retains only 47% of its 1 C capacity (**Figure 2c**),
20 which can be attributed to the bulk particle sizes of VOPO₄·2H₂O. Note that at 10 C rate, the
21 IPB electrode retains 84% of its 1 C capacity for the Fe²⁺ storage, where the particle sizes of
22 the IPB electrode are below 100 nm.^[17] As a comparison, the rate performance of
23 VOPO₄·2H₂O storing Zn²⁺ is also studied, as shown in **Figure S5**, where VOPO₄·2H₂O
24 retains 35% of its 1 C capacity at 10 C, more sluggish than the storage of Fe²⁺.

25 To further examine the kinetics of Fe²⁺ (de)intercalation, galvanostatic intermittent
26 titration technique (GITT) was employed to calculate the diffusion coefficient over the

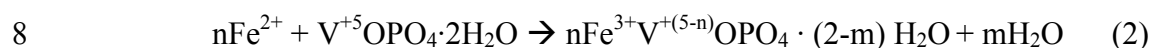
1 charging process, which reveals the diffusivity ranging from $1\text{E-}13 \sim 1\text{E-}11 \text{ cm}^2/\text{s}$, as shown in
2 **Figure 2d** and **Figure S6**. Such diffusivity resembles that of VOPO_4 when storing Zn^{2+} from
3 aqueous electrolytes.^[38] Interestingly, the diffusion coefficient continuously decreases with
4 the increase of the cell potential. The slower kinetics at higher potentials is corroborated by
5 the results of electrochemical impedance spectroscopy (EIS). As shown in **Figure 2e**, R_{ct}
6 gradually increases from 6.9Ω (at 0 V) to 8.1Ω (at 0.9 V). The results imply that the initial
7 removal of Fe^{2+} renders further extraction of Fe^{2+} more difficult; thus, we can deduce that the
8 initial intercalation of Fe^{2+} can facilitate the diffusion of forthcoming Fe^{2+} intercalation.

9 $\text{VOPO}_4 \cdot 2\text{H}_2\text{O}$ exhibits much more stable cycling performance in 1 M FeSO_4 than in 1
10 M ZnSO_4 (**Figure 2f**). $\text{VOPO}_4 \cdot 2\text{H}_2\text{O}$ electrode retains 81% of its initial capacity after 50
11 cycles at 1 C in 1 M FeSO_4 , whereas in the ZnSO_4 electrolyte, the specific capacity fades to
12 28% within 50 cycles. The $\text{VOPO}_4 \cdot 2\text{H}_2\text{O}$ as an electrode usually shows poor cycling
13 performance for hosting multi-valence charge carriers, *e.g.*, Mg^{2+} , Ca^{2+} , and Zn^{2+} , because the
14 (de)insertion of multivalent charge carriers causes the exfoliation of the layered structure
15 assembled by the weak *van der Waals* forces.^[12, 31, 40] The stable cycling performance in
16 FeSO_4 is surprising since one would expect similar capacity decaying performance for hosting
17 Fe^{2+} and Zn^{2+} alike, given that they have the same charge (2+) and similar ionic radii (70 pm
18 for Fe^{2+} vs. 74 pm for Zn^{2+}).^[17]

19 Interestingly, soaking the $\text{VOPO}_4 \cdot 2\text{H}_2\text{O}$ electrode in the FeSO_4 electrolyte alters its
20 XRD pattern, suggesting the formation of a new phase, where the (001) peak of $\text{VOPO}_4 \cdot 2\text{H}_2\text{O}$
21 shifts from 12.8° to 13.8° , corresponding to the drastic contraction of the interlayers with d-
22 spacing decreasing from 6.94 \AA to 6.42 \AA (**Figure 3b**). The lattice contraction indicates that
23 by soaking the electrode in the electrolyte, Fe-ions are inserted into the electrode structure in
24 an electroless redox reaction, where, as a result, the inserted Fe-ions pull the adjacent layers
25 closer. Interestingly, soaking of the electrode may cause the expulsion of lattice water, as
26 suggested by the subsided FTIR peaks of the electrode at $\sim 3580 \text{ cm}^{-1}$ and $\sim 1580 \text{ cm}^{-1}$

1 **(Figure 3d)**. Furthermore, after soaking, both V=O stretching (875.6 cm^{-1}) and P-O stretching
 2 (1072.3 cm^{-1}) of the VOPO_4 framework blue-shift from 875.6 cm^{-1} to 962.7 cm^{-1} and from
 3 1072.3 cm^{-1} to 1143.9 cm^{-1} , respectively, suggesting the shortened bonds due to the removal
 4 of lattice water molecules.

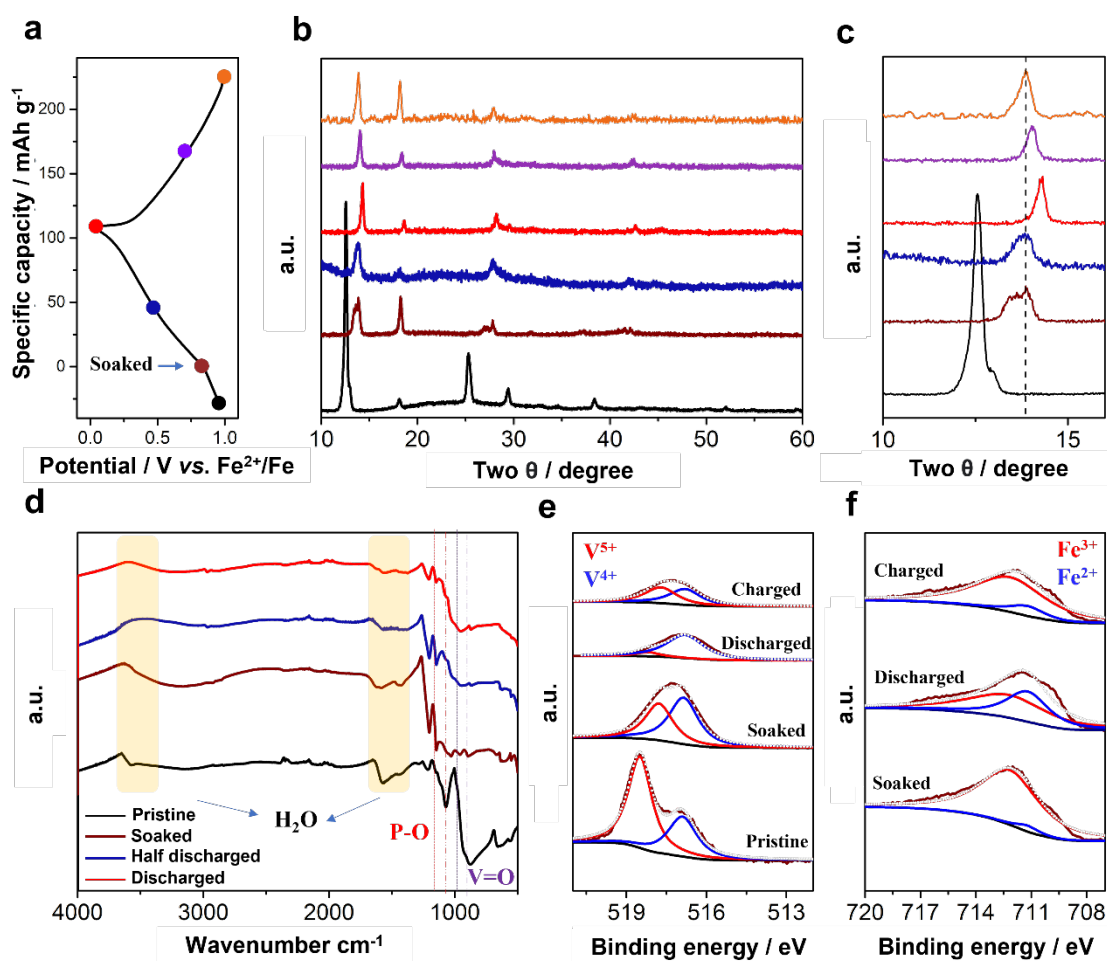
5 Another piece of evidence of spontaneous Fe-ion insertion into the structure is that the
 6 OCV of the resting cells decreases, which indicates the reduction of the $\text{VOPO}_4 \cdot 2\text{H}_2\text{O}$
 7 electrode. It can be described by the following chemical reaction:



9 where vanadium (+5) is reduced to a lower oxidation state, and Fe^{2+} is oxidized to Fe^{3+} . In
 10 order to compensate for the charge neutrality, Fe^{3+} ought to be inserted into the lattice of
 11 $\text{VOPO}_4 \cdot 2\text{H}_2\text{O}$. Thus, the uniquely stable cycling performance of Fe^{2+} storage relates to the
 12 electroless redox reaction between the $\text{VOPO}_4 \cdot 2\text{H}_2\text{O}$ electrode and Fe^{2+} once the electrode
 13 touches the electrolyte, where the inserted Fe^{3+} stabilizes the structure of the $\text{VOPO}_4 \cdot 2\text{H}_2\text{O}$
 14 electrode. *Ex situ* XPS spectra of the pristine and the soaked electrode provide unequivocal
 15 evidence for the postulation that Fe^{2+} from the electrolyte is oxidized to Fe^{3+} that is
 16 consecutively inserted into the structure of VOPO_4 (**Figure 3e, f**). After soaking, the iron
 17 signal is predominantly Fe^{3+} and the soaking process reduces some of the V^{5+} to V^{4+} .

18 The capacity “deficit” of the first discharge compared to the second discharge can be
 19 used to evaluate how much Fe^{3+} is inserted into the $\text{VOPO}_4 \cdot 2\text{H}_2\text{O}$ electrode before cycling.
 20 This capacity difference of 23 mAh/g suggests a formula of $\text{Fe}_{0.04}\text{VOPO}_4 \cdot 2\text{H}_2\text{O}$. In order to
 21 gain a better understanding of the pre-intercalation of Fe^{3+} , we carried out electrochemical
 22 quartz crystal microbalance (EQCM) measurements during the cell resting at OCV (**Figure**
 23 **S7**). The frequency of the quartz crystal decreases, suggesting the mass addition of the
 24 electrode during its soaking in the electrolyte due to the intercalation of Fe^{3+} . The calculated
 25 mass change of the electrode corresponds to a stoichiometry of $\text{Fe}_{0.05}\text{VOPO}_4 \cdot 2\text{H}_2\text{O}$, which is
 26 in line with the capacity-based estimation.

1



2

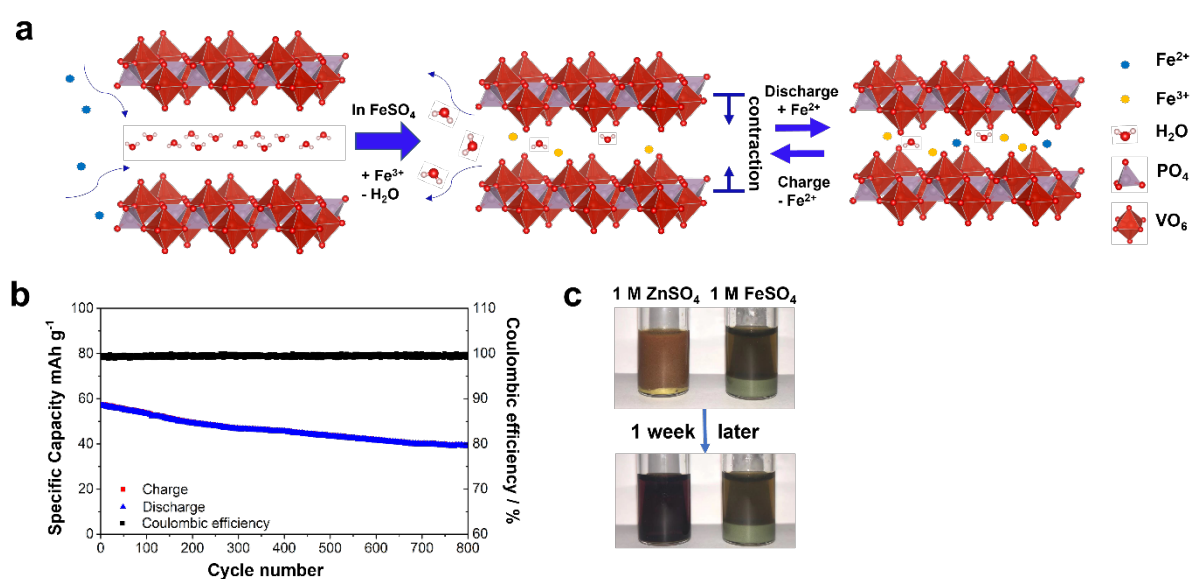
3 **Figure 3** (a) GCD profiles of a free-standing film electrode of $\text{VOPO}_4 \cdot 2\text{H}_2\text{O}$ with an active
 4 mass loading of 9 mg/cm^2 at 5 mA/g (b) *Ex situ* XRD patterns of the $\text{VOPO}_4 \cdot 2\text{H}_2\text{O}$ electrode
 5 at different SOC, which are color-coded corresponding to (a). (c) An enlarged view of the
 6 (001) peak. (d) *Ex situ* FTIR spectra at different SOC (dashed line: before soaking; solid line:
 7 after soaking). XPS spectra of electrodes for (e) V $2p_{3/2}$ and (f) Fe $2p_{3/2}$ at different SOC.

8

9 As shown in XRD patterns (**Figure 3c**), the discharge process causes the structure to
 10 further contract along the [001] direction continuously, where the (001) interlayer d-spacing
 11 shrinks from 6.42 \AA to 6.16 \AA upon the full discharge. Upon charging, the structure reversibly
 12 expands back to the (001) d-spacing of the soaked electrode but not to that of the pristine dry
 13 electrode, suggesting good structural elasticity and the trapping of Fe^{3+} inserted during

1 soaking. Interestingly, the discharge process does not vary the positions of the peaks of P-O
 2 and V=O in the FTIR spectra, which suggests a lack of bonding covalency between the
 3 inserted Fe^{2+} ions and the host framework. *Ex situ* XPS results reveal the valence changes of
 4 V and Fe during the GCD processes, as shown in **Figure 3e, f**. The first discharge process
 5 renders V^{5+} nearly completely reduced to V^{4+} and brings in much Fe^{2+} . The following charge
 6 eliminates most of the Fe^{2+} from the electrode; however, even after the electrode is fully
 7 charged, there still exists significant presence of V^{4+} due to the trapping of Fe^{3+} in the
 8 electrode.

9 To this point, a mechanism surfaces, as illustrated in **Figure 4a**. Briefly, $\text{VOPO}_4 \cdot 2\text{H}_2\text{O}$
 10 takes in and traps Fe^{3+} upon touching the electrolyte, which contracts the lattice and expels
 11 some of the lattice water. During the subsequent discharge process, the intercalation of Fe^{2+}
 12 causes further structural contraction between the (001) layers. This structural contraction due
 13 to the electrochemical Fe^{2+} insertion can be reversed in the following charge process.
 14 However, this charge process cannot reverse the structural changes of the electrode caused by
 15 the electrode soaking, which suggests that the pre-intercalation of Fe^{3+} is permanent, and
 16 these ions are trapped in the structure throughout cycling.



17

1 **Figure 4** (a) Schematic of Fe^{3+} pre-intercalation mechanism and the following Fe^{2+}
2 charge/discharge process (The $\text{Fe}^{3+}/\text{Fe}^{2+}$ ratio should not be taken literally). (b) Cycling
3 performance of Fe^{2+} storage at 8 C. (c) Digital images of $\text{VOPO}_4 \cdot 2\text{H}_2\text{O}$ soaked in 1 M FeSO_4
4 and 1 M ZnSO_4 before (top) and after one week (bottom).

5
6 We further examined the cycling stability of $\text{VOPO}_4 \cdot 2\text{H}_2\text{O}$ for Fe^{2+} storage, **Figure 4b**
7 shows the cycling performance of $\text{VOPO}_4 \cdot 2\text{H}_2\text{O}$ in the FeSO_4 electrolyte at 8 C, where the
8 electrode exhibits stable cycling for 800 cycles with 65% capacity retention. The cycling
9 results offer additional evidence for the mechanism of Fe-ion storage in $\text{VOPO}_4 \cdot 2\text{H}_2\text{O}$, where
10 the trapped Fe^{3+} ions provide ionic bonding between the layers, thus bolting the structure and
11 making it difficult to exfoliate. Chemical stability of $\text{VOPO}_4 \cdot 2\text{H}_2\text{O}$ powder in 1 M FeSO_4 and
12 1 M ZnSO_4 electrolytes can be differentiated by a soaking process. As shown in **Figure 4c**,
13 after one week, $\text{VOPO}_4 \cdot 2\text{H}_2\text{O}$ (100 mg) is largely dissolved in 3 ml 1 M ZnSO_4 , rendering a
14 solution dark red. In contrast, the $\text{VOPO}_4 \cdot 2\text{H}_2\text{O}$ powder remains as solid in 1 M FeSO_4 after
15 soaking.

16 The mechanism of slow capacity fading for storing Fe^{2+} is speculated to be the
17 oxidation of Fe^{2+} in the electrolyte as side reactions. As shown in **Figure S8a**, the separator
18 collected after 300 cycles shows the color of brown precipitation, indicating the presence of
19 Fe^{3+} due to the oxidation of the electrolyte. The capacity of the cycled electrode is restored
20 after the cycled electrode is rinsed and put into a new cell with the fresh FeSO_4 electrolyte
21 (**Figure S8b**). Note that the Swagelok cells we used for the tests are not as hermetic as pouch
22 cells or coin cells. Therefore, provided that the iron batteries are better sealed, the cycling life
23 of such batteries can be significantly provided.

24 Fe-ion batteries with Fe^{2+} as a charge carrier holds a unique position in aqueous
25 batteries research due to the extremely low cost and abundance of Fe. However, this battery
26 chemistry also has its own drawbacks compared to other aqueous batteries such as the

1 sensitivity of the Fe^{2+} electrolyte to air and the upper limit of the cathode's operation potential
2 that should not be high enough to oxidize Fe^{2+} . In addition, to date, the plating/stripping of Fe
3 metal anode has yet not demonstrated a high CE comparable to that of Zn metal anode. To
4 better illustrate the pros and cons of this emerging battery, **Table S1** is provided in the
5 Supporting Information, where the potentially developed Fe-ion batteries are compared with
6 other aqueous storage batteries. The message is that Fe-ion batteries would potentially be
7 competitive with other aqueous batteries by its low cost rather than by its energy density,
8 provided that its long cycle life can be secured with highly reversible Fe metal anode.

9 **3. Conclusion**

10 In summary, we demonstrated that $\text{VOPO}_4 \cdot 2\text{H}_2\text{O}$ can be a suitable Fe-ion battery cathode
11 with a specific capacity of ~ 100 mAh/g, an average potential of ~ 0.6 V, and most importantly
12 stable cycling life. In the FeSO_4 electrolyte, there takes place a unique pre-insertion
13 mechanism due to the spontaneous oxidation of Fe^{2+} by the electrode and the associated
14 insertion of Fe^{3+} into $\text{VOPO}_4 \cdot 2\text{H}_2\text{O}$. The pre-inserted Fe^{3+} ions are trapped in the structure and
15 play a role of bolting the structure for the reversible storage of Fe^{2+} in the following cycling.
16 Such an iron-bolting mechanism sheds light on a strategy to use trapped ions to stabilize
17 layered structures as electrodes for multi-valent ion batteries.

18

19 **4. Experimental section**

20 *Preparation of $\text{VOPO}_4 \cdot 2\text{H}_2\text{O}$:*

21 $\text{VOPO}_4 \cdot 2\text{H}_2\text{O}$ was synthesized according to a reported reflux method. The mixture, including
22 V_2O_5 (4.8 g), H_3PO_4 (85%, 26.6 ml), and H_2O (115.4 ml), was refluxed for 16 hr at 110 °C.
23 The system was then cooled down to room temperature, and the yellow precipitate was
24 collected for centrifuge, three times with water and one last time with ethanol. The resulting
25 product was dried in oven at 60 °C for 3 hr.

26

1 *Material characterization:*

2 XRD patterns were collected on a Rigaku Ultima IV diffractometer with Cu K α radiation ($\lambda =$
3 1.5406 Å). Morphology studies were done on an FEI NOVA 230 high-resolution SEM. FTIR
4 results were collected on a NICOLET 5397 AVATAR 360 FTIR spectrometer. Crystal water
5 content of VOPO₄·2H₂O was determined from TGA (SDTQ600), and vanadium valence
6 states were determined from XPS (Thermo Scientific K-Alpha+).

7

8 *Electrochemical characterization:*

9 The working electrode comprises 70 wt% VOPO₄·2H₂O active mass, 20 wt% Ketjen black
10 (KB) carbon, and 10 wt% polyvinylidene fluoride (PVdF) binder. Carbon fiber paper
11 (FuelCellsEtc Company) was used as a current collector. The counter/reference electrode is
12 composed of 80 wt% Fe powder, 10 wt% KB, and 10 wt% PVdF as binder. In order to
13 prevent the oxidation of Fe powder, the slurry was casted on carbon paper in a nitrogen-filled
14 glovebox and dried in vacuum oven at 50 °C. To prepare the FeSO₄ electrolyte, the deionized
15 water was acidified to pH= 5.5 using 0.1 m H₂SO₄ followed by N₂ purging for 2 hr to
16 eliminate the dissolved O₂. The acidified and de-gassed water was transferred to the nitrogen-
17 filled glovebox to prepare the 1 M FeSO₄ electrolyte, and small amount of Fe powder was
18 added to the electrolyte solution for the prevention of FeSO₄ oxidation. To prevent Fe powder
19 and FeSO₄ oxidation, all three-electrode Swagelok cells and two-electrode coin cells were
20 assembled in a nitrogen-filled glovebox. The CV was done on a VMP-3 multichannel
21 workstation. The GCD, rate, cycling performance were tested on an Arbin BT2000 battery
22 cycler.

23

24 *Electrochemical quartz crystal microbalance experiments (EQCM):*

25 EQCM was conducted on a QCM200 quartz crystal microbalance. A slurry composed of 7 mg
26 of VOPO₄·2H₂O, 2 mg of KB, and 3 mg of PVdF in 600 μ l NMP was sonicated for 4 hr. After

1 sonication it was sprayed onto a 1-inch quartz crystal disk (O100RX3, p/n 6-615 Ti/Au, 5
 2 MHz). The frequency changes of the quartz resonator (Δf) and the corresponding mass
 3 changes (Δm) were related by the Sauerbrey's equation:

$$4 \quad \Delta m = \frac{\sqrt{\rho_q \mu_q}}{2f_0} * \Delta f = -C_f * \Delta f$$

5 where ρ_q is the density of quartz (2.648 g/cm³), μ_q is the shear modulus of quartz (2.947 ×
 6 1011 g/cm s²), f_0 is the fundamental resonance frequency of the quartz, C_f is the sensitivity
 7 factor, and Δm and Δf are the mass change and frequency change, respectively. C_f is obtained
 8 by calculating the relation based on frequency and mass changes between clean quartz and the
 9 coated electrodes. The value of the calibration constant used in this work is 13 ng/Hz.

10
 11
 12
 13
 14

Supporting Information

Supporting Information is available from the Wiley Online Library or from the author.

Acknowledgements

16 X. Ji thanks National Science Foundation for the financial support with Award No. CBET-
 17 2038381. The authors thank Oregon State University EM facility for SEM and EDX mapping
 18 measurements. The authors are grateful to Dr. May Nyman for the measurements of TGA.

19
 20
 21
 22
 23
 24
 25
 26

Received: ((will be filled in by the editorial staff))
 Revised: ((will be filled in by the editorial staff))
 Published online: ((will be filled in by the editorial staff))

References

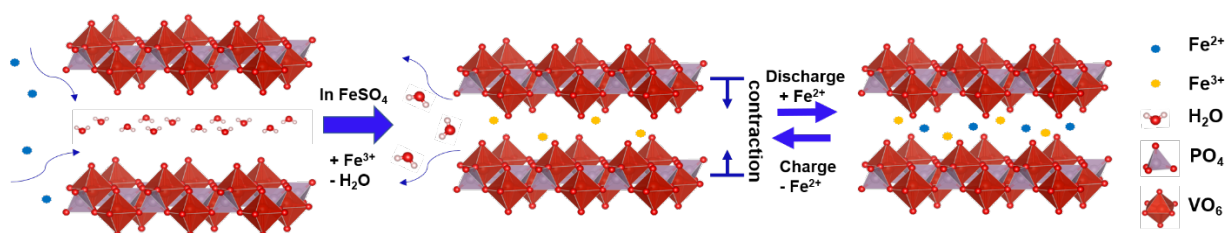
- 28 [1] D. Bin, F. Wang, A. G. Tamirat, L. Suo, Y. Wang, C. Wang, Y. Xia, *Advanced Energy*
 29 *Materials*, **2018**, 8, 1703008.
 30 [2] Y. Zhang, F. Wan, S. Huang, S. Wang, Z. Niu, J. Chen, *Nature communications*, **2020**,
 31 11, 1.
 32 [3] C. Zhao, Q. Wang, Z. Yao, J. Wang, B. Sánchez-Lengeling, F. Ding, X. Qi, Y. Lu, X.
 33 Bai, B. Li, H. Li, A. Aspuru-Guzik, X. Huang, C. Delmas, M. Wagemaker, L. Chen,
 34 Y. Hu, *Science*, **2020**, 370, 708.
 35 [4] Y. Dai, X. Liao, R. Yu, J. Li, J. Li, S. Tan, P. He, Q. An, Q. Wei, L. Chen, X. Hong,
 36 K. Zhao, Y. Ren, J. Wu, Y. Zhao, L. Mai, *Advanced Materials*, **2021**, 2100359.

- 1 [5] W. Sun, F. Wang, B. Zhang, M. Zhang, V. Küpers, X. Ji, C. Theile, P. Bieker, K. Xu,
2 C. Wang, *Science*, **2021**, 371, 46.
- 3 [6] J. Qian, X. Wu, Y. Cao, X. Ai, H. Yang, *Angewandte Chemie*, **2013**, 125, 4731.
- 4 [7] H. Pan, Y. Shao, P. Yan, Y. Cheng, K. S. Han, Z. Nie, C. Wang, J. Yang, X. Li, P.
5 Bhattacharya, K. T. Mueller, J. Liu, *Nature Energy*, **2016**, 1, 16039.
- 6 [8] Q. Yang, G. Liang, Y. Guo, Z. Liu, B. Yan, D. Wang, Z. Huang, X. Li, J. Fan, C. Zhi,
7 *Advanced Materials*, **2019**, 31, 1903778.
- 8 [9] C. Xu, B. Li, H. Du, F. Kang, *Angewandte Chemie International Edition* **2012**, 51,
9 933.
- 10 [10] Y. Sui, X. Ji, *Chemical Reviews*, **2021**, 121, 11, 6654–6695
- 11 [11] C. Zhang, W. Shin, L. Zhu, C. Chen, J. C. Neufeind, Y. Xu, S. I. Allec, C. Liu, Z.
12 Wei, A. Daniyar, J.-X. Jiang, C. Fang, P. Alex Greaney, X. Ji, *Carbon*
13 *Energy*. **2021**; 3: 339– 348.
- 14 [12] F. Wang, W. Sun, Z. Shadike, E. Hu, X. Ji, T. Gao, X.-Q. Yang, K. Xu, C. Wang,
15 *Angewandte Chemie International Edition*, **2018**, 57, 11978.
- 16 [13] V. Verma, S. Kumar, W. Manalastas, J. Zhao, R. Chua, S. Meng, P. Kidkhunthod, M.
17 Srinivasan, *ACS Applied Energy Materials*, **2019**, 2, 8667.
- 18 [14] G. Fang, J. Zhou, A. Pan, S. Liang, *ACS Energy Letters*, **2018**, 3, 2480.
- 19 [15] X. Zhang, D. Yang, W. Liu, X. Rui, *Frontiers in Energy Research*, **2020**, 8.
- 20 [16] Z. Guo, Y. Ma, X. Dong, J. Huang, Y. Wang, Y. Xia, *Angewandte Chemie*
21 *International Edition*, **2018**, 57, 11737.
- 22 [17] X. Wu, A. Markir, Y. Xu, C. Zhang, D. P. Leonard, W. Shin, X. Ji, *Advanced*
23 *Functional Materials*, **2019**, 29, 1900911.
- 24 [18] M. A. Miller, J. S. Wainright, R. F. Savinell, *Journal of The Electrochemical Society*,
25 **2017**, 164, A796.
- 26 [19] T. A. Edison, US1379088A, **1901**.
- 27 [20] A. K. Manohar, C. Yang, S. Malkhandi, B. Yang, G. S. Prakash, S. Narayanan,
28 *Journal of the Electrochemical Society*, **2012**, 159, A2148.
- 29 [21] X. Yu, A. Manthiram, *ACS Energy Letters*, **2017**, 2, 1050.
- 30 [22] D. Lei, D. Lee, A. Magasinski, E. Zhao, D. Steingart, G. Yushin, *ACS applied*
31 *materials interfaces*, **2016**, 8, 2088.
- 32 [23] W. Sun, F. Wang, S. Hou, C. Yang, X. Fan, Z. Ma, T. Gao, F. Han, R. Hu, M. Zhu, C.
33 Wang, *Journal of the American Chemical Society*, **2017**, 139, 9775.
- 34 [24] M. Yan, P. He, Y. Chen, S. Wang, Q. Wei, K. Zhao, X. Xu, Q. An, Y. Shuang, Y.
35 Shao, K. T. Mueller, L. Mai, J. Liu, J. Yang, *Advanced Materials*, **2018**, 30, 1703725.
- 36 [25] N. Zhang, X. Chen, M. Yu, Z. Niu, F. Cheng, J. Chen, *Chemical Society Reviews*,
37 **2020**, 49, 4203.
- 38 [26] X. Wu, A. Markir, Y. Xu, E. C. Hu, K. T. Dai, C. Zhang, W. Shin, D. P. Leonard, K.
39 Kim, X. Ji, *Advanced Energy Materials*, **2019**, 9, 1902422.
- 40 [27] V. K. Saroja, A. P. Samantaray, S.S. Sundara, Ramaprabhu, *Chemical*
41 *Communications*, **2019**, 55, 10416.
- 42 [28] Y. Lu, T. Zhu, W. van den Bergh, M. Stefik, K. Huang, *Angewandte Chemie*
43 *International Edition*, **2020**, 59, 17004.
- 44 [29] L. Zhou, Q. Liu, Z. Zhang, K. Zhang, F. Xiong, S. Tan, Q. An, Y. Kang, Z. Zhou, L.
45 Mai, *Advanced Materials*, **2018**, 30, 1801984.
- 46 [30] C. Wu, X. Lu, L. Peng, K. Xu, X. Peng, J. Huang, G. Yu, Y. Xie, *Nature*
47 *Communications*, **2013**, 4, 2431.
- 48 [31] X. Ji, J. Chen, F. Wang, W. Sun, Y. Ruan, L. Miao, J. Jiang, C. Wang, *Nano Letters*,
49 **2018**, 18, 6441.

- 1 [32] B. E. Conway, *Electrochemical supercapacitors: scientific fundamentals and*
 2 *technological applications*, Springer Science & Business Media, **2013**.
 3 [33] V. Augustyn, P. Simon, B. J. E. Dunn, E. *Science*, **2014**, 7, 1597.
 4 [34] S. Li, Y. Luo, W. Lv, W. Yu, S. Wu, P. Hou, Q. Yang, Q. Meng, C. Liu, H. Cheng,
 5 *Advanced Energy Materials*, **2011**, 1, 486.
 6 [35] L. Qie, W. Chen, Z. Wang, Q. Shao, X. Li, L. Yuan, X. Hu, W. Zhang, Y. Huang,
 7 *Advanced Materials*, **2012**, 24, 2047.
 8 [36] Z. Chen, V. Augustyn, X. Jia, Q. Xiao, B. Dunn, Y. Lu, *ACS Nano*, **2012**, 6, 4319.
 9 [37] J. Wang, J. Polleux, J. Lim, B. Dunn, *The Journal of Physical Chemistry C*, **2007**, 111,
 10 14925.
 11 [38] M. Liao, J. Wang, L. Ye, H. Sun, Y. Wen, C. Wang, X. Sun, B. Wang, H. Peng,
 12 *Angewandte Chemie International Edition*, **2020**, 59, 2273.
 13 [39] W. Liu, L. Dong, B. Jiang, Y. Huang, X. Wang, C. Xu, Z. Kang, J. Mou, F. Kang,
 14 *Electrochimica Acta*, **2019**, 320, 134565.
 15 [40] J. Wang, S. Tan, F. Xiong, R. Yu, P. Wu, L. Cui, Q. An, *Chemical Communications*,
 16 **2020**, 56, 3805.
 17
 18
 19

The table of contents

Iron ion batteries are promising for grid energy storage due to their low cost and compatibility with aqueous electrolytes. This work demonstrates vanadium oxyphosphate as a capable cathode to host Fe^{2+} . Vanadium oxyphosphate exhibits structural stability favoring Fe^{2+} to Zn^{2+} due to the bolting effect by the pre-intercalated Fe^{3+} before battery cycling.



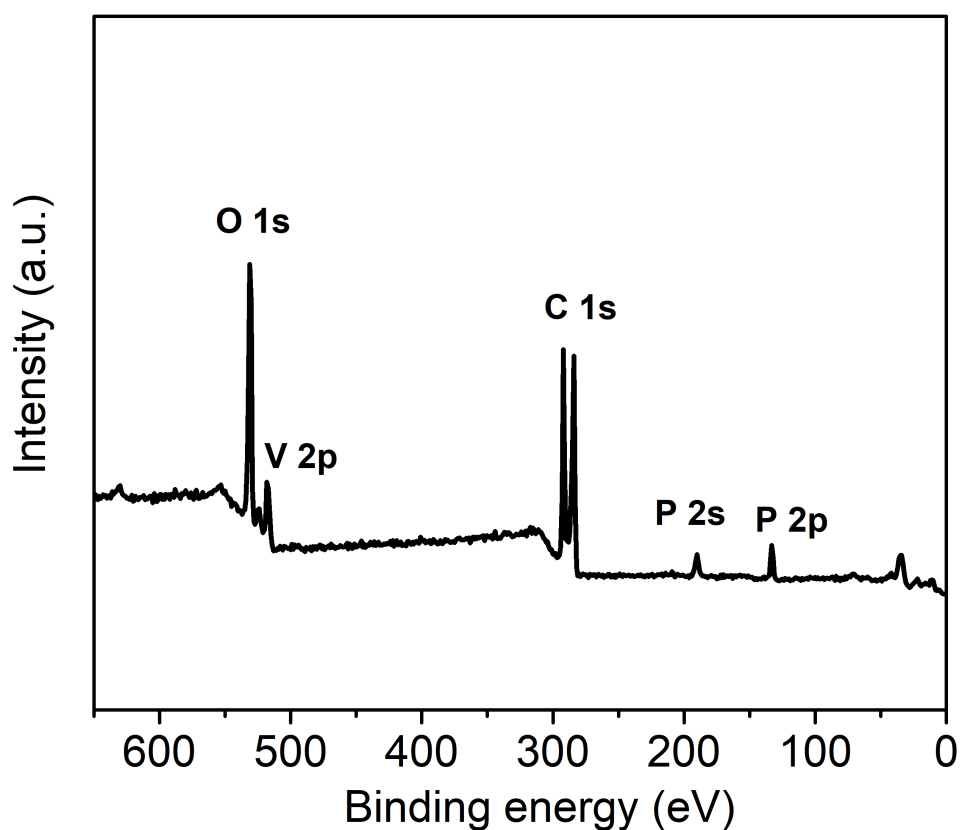
Supporting Information

Iron-Ion Bolted $\text{VOPO}_4 \cdot 2\text{H}_2\text{O}$ as an Aqueous Fe-ion Battery Electrode

Yunkai Xu, Xianyong Wu, Sean K. Sandstrom, Jessica J. Hong, Heng Jiang, Xin Chen, Xiulei

Ji*

Y. Xu, Dr. X. Wu, S. K. Sandstrom, J. J. Hong, Dr. H. Jiang, Dr. X. Chen, Prof. X. Ji
Department of Chemistry
Oregon State University
Corvallis, OR 97331, USA
E-mail: david.ji@oregonstate.edu

**Figure S1** Full XPS spectrum of $\text{VOPO}_4 \cdot 2\text{H}_2\text{O}$.

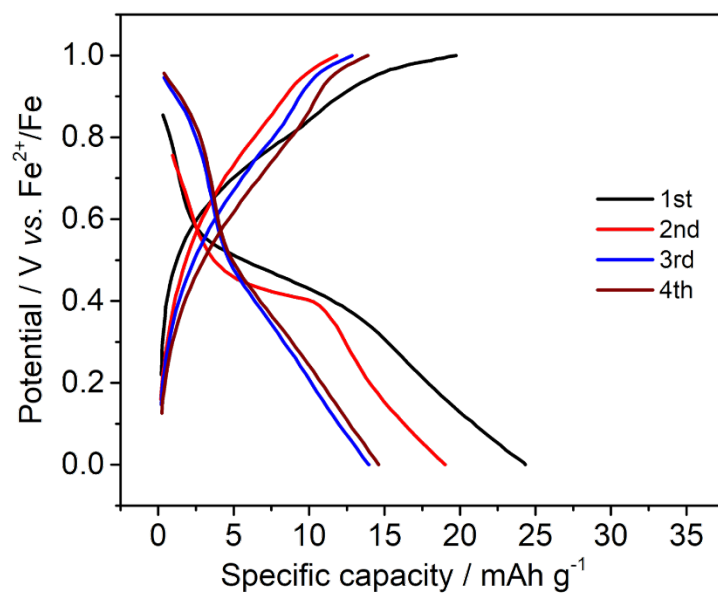


Figure S2 GCD potential profiles of VOPO₄·2H₂O in 3 mM H₂SO₄ at 100 mA g⁻¹.

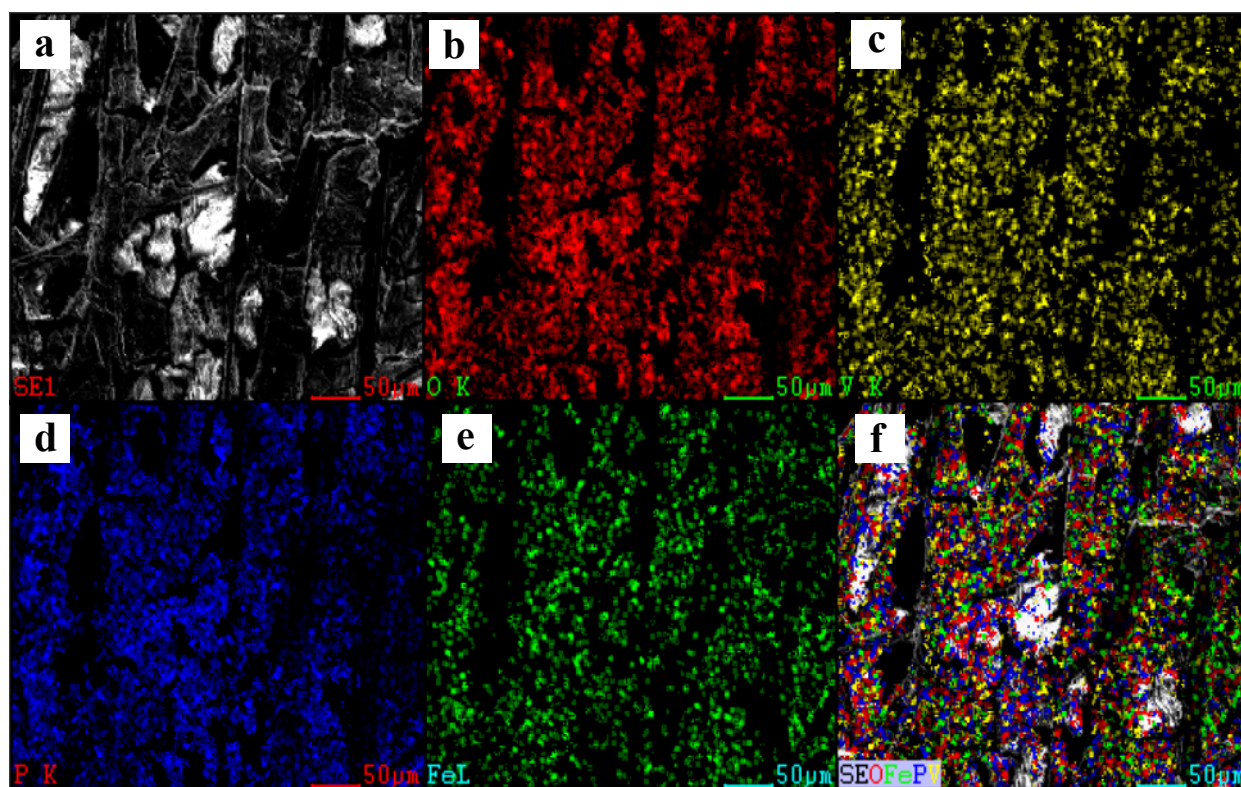


Figure S3 The SEM and EDX elemental mappings of the discharged $\text{VOPO}_4 \cdot 2\text{H}_2\text{O}$ electrode. (a) SEM image. (b), (c), (d), and (e) Elemental mappings of oxygen, vanadium, phosphorus, and iron. (f) Overlapped elemental mappings.

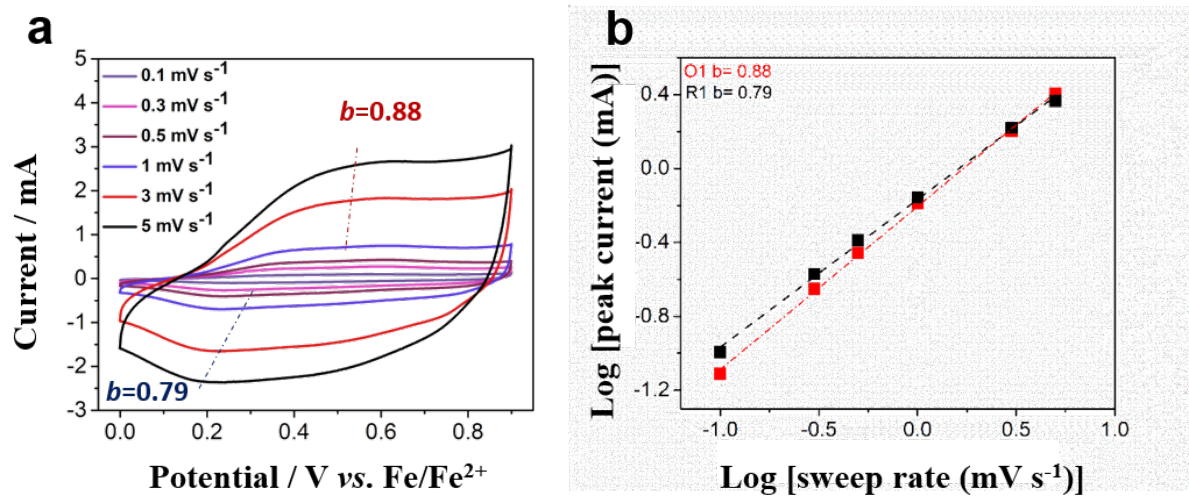


Figure S4 (a) CV of the VOPO₄·2H₂O electrode for the storage of Fe²⁺ collected at different scan rates. (b) The calculated b -values from CV at different scan rates.

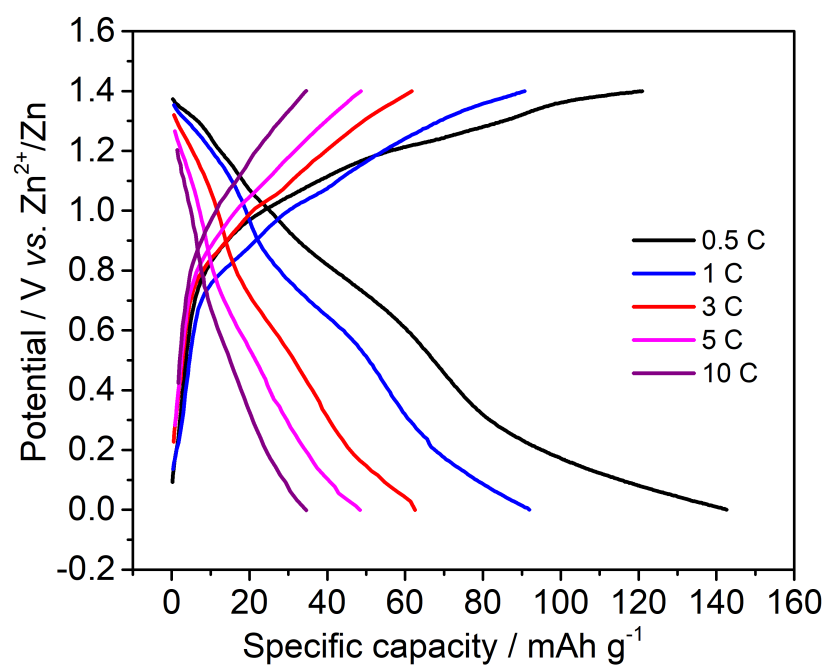


Figure S5 GCD potential profiles of the VOPO₄·2H₂O electrode storing Zn²⁺ at different C-rates.

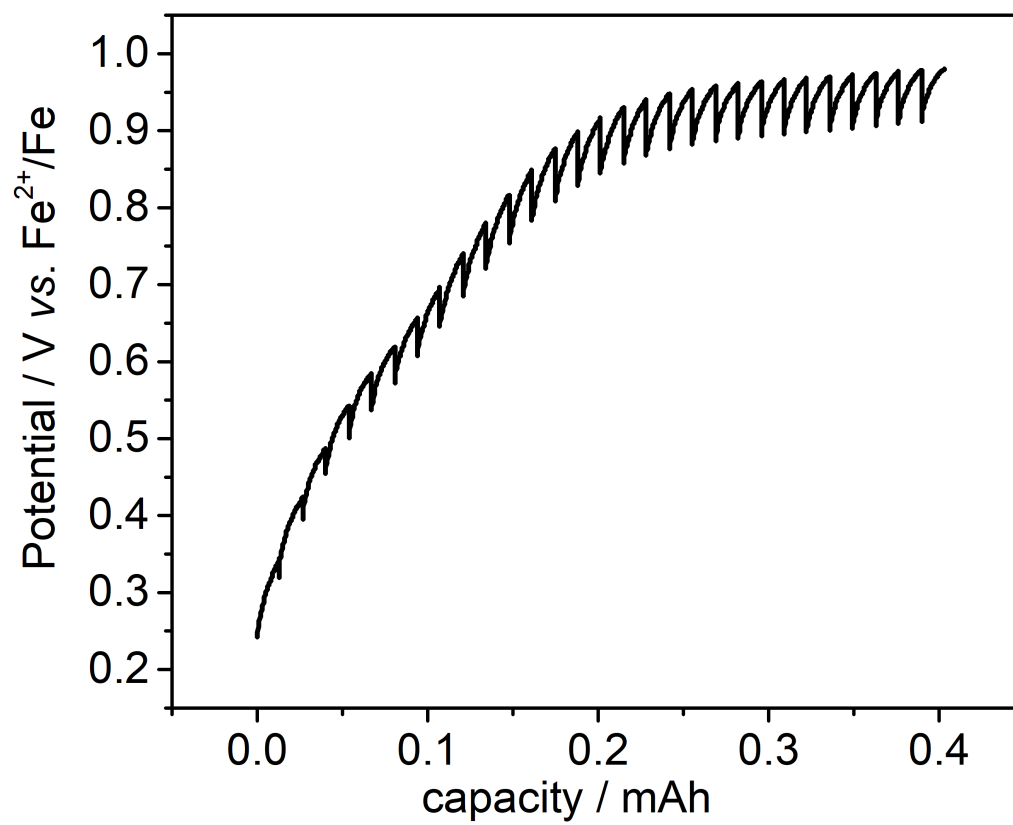


Figure S6 GITT profile of VOPO₄·2H₂O in the 1 M FeSO₄ electrolyte for the charge process.

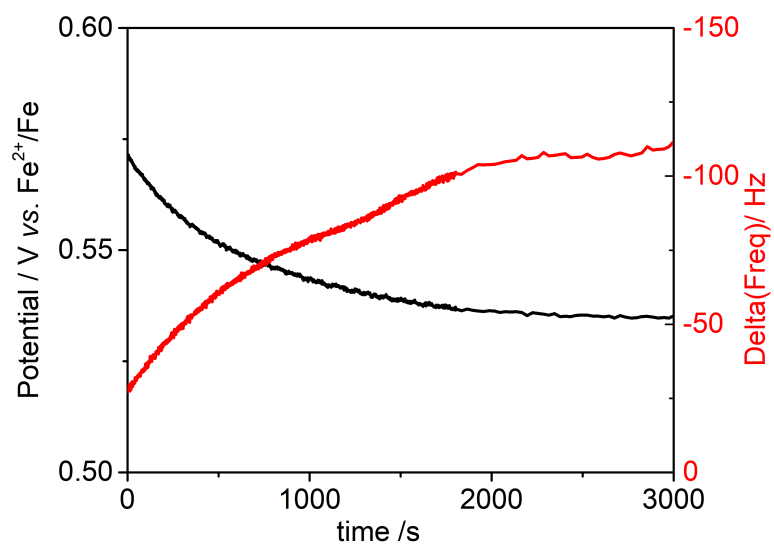


Figure S7 EQCM and potential profiles as a function of time for the VOPO₄·2H₂O electrode during soaking in the 1 M FeSO₄ electrolyte.

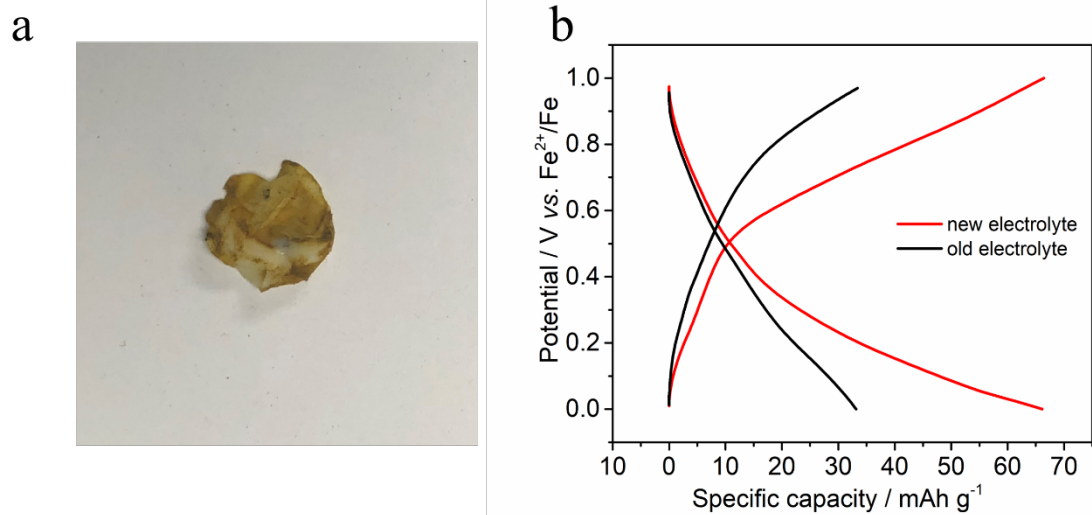


Figure S8 (a) Digital image of a separator after 300 cycles. (b) GCD potential profiles of the cycled electrode before (black) and after (red) replacing the electrolyte with freshly made FeSO_4 electrolyte.

Table S1. Techno-economic characteristics of major aqueous storage batteries from a full cell's point of view.

Batteries	Showstopper	Energy density (Wh/kg)	Cell Voltage	Cycle life	Air sensitive or not	Potential levelized energy cost
Lead-acid ⁽¹⁾	Cycling	30	High	300 to 1000	No	Medium
NiMH ⁽²⁾	Rare earth metals	80-100	Medium	>1000	No	Medium
Flow batteries ⁽³⁾	Non-modular	~20	Low	>5000	Yes	Low
Zn metal batteries (Zn//MnO ₂) ^{* (4)}	Unknown	~100	Medium	To be revealed	No	Medium
Iron-ion batteries*	Unknown	~50	Low	To be revealed	Yes	Low

* Calculation based on n/p capacity ratio of 1.2/1.

References

- [1] P. Ruetschi, *Journal of Power Sources*, **1977**, 2, 3.
- [2] M. Fetcenko, S. Ovshinsky, B. Reichman, K. Young, C. Fierro, J. Koch, A. Zallen, W. Mays, T. Ouchi, *Journal of Power Sources*, **2007**, 165, 544.
- [3] M. Skyllas-Kazacos, M. Chakrabarti, S. Hajimolana, F. Mjalli, M. Saleem, *Journal of the electrochemical society*, **2011**, 158, R55.
- [4] H. Pan, Y. Shao, P. Yan, Y. Cheng, K. S. Han, Z. Nie, C. Wang, J. Yang, X. Li, P. Bhattacharya, K. T. Mueller, J. Liu, *Nature Energy*, **2016**, 1, 16039.